RSC Advances

PAPER

View Article Online
View Journal | View Issue

Cite this: *RSC Adv.*, 2022, **12**, 25898

Template and interfacial reaction engaged synthesis of $CeMnO_x$ hollow nanospheres and their performance for toluene oxidation†

Yuhua Zheng,[a] Jing Zhou,[c] Xi Zeng,[b] Dandan Hu,[a] Fang Wang[b] and Yanbin Cui *[a]

Received 27th July 2022
Accepted 5th September 2022

DOI: 10.1039/d2ra04678d

rsc.li/rsc-advances

A series of well-dispersed $CeMnO_x$ hollow nanospheres with uniform diameter and thickness were synthesized by a novel approach combining the template method and interfacial reaction. A SiO_2 template was used as a hard template for preparation of SiO_2@CeO_2 nanospheres by solvothermal reaction. SiO_2@$CeMnO_x$ could be formed after $KMnO_4$ was reacted with SiO_2@CeO_2 by interfacial reaction between MnO_4^- and Ce^{3+}. Among all the prepared catalysts, $CeMnO_x$-3 with a moderate content of Mn (15 wt%) exhibited the lowest temperature for complete combustion of toluene (280 °C). Moreover, it showed high stability for 36 h with toluene conversion above 97.7% and good water tolerance with 5 vol% H_2O. With characterization, we found that the reaction between Ce and Mn in the Ce–Mn binary oxides gave rise to increased Ce^{3+} and oxygen vacancies, which led to the formation of enhanced reducibility and more surface-absorbed oxygens (O_2^{2-}, O^{2-} and O^-), and improved the catalytic performance further.

1 Introduction

As one of the primary sources of air pollutants, volatile organic compounds (VOCs) are not only significant contributors to smog formation, but also can cause environmental pollution and bring great negative effects to human health.[1,2] Some VOCs have been classified as carcinogens, such as benzene, toluene, dichloromethane, and dichloroethane.[3] Therefore, the effective removal of VOCs has been an important research topic in environmental governance.

Numerous methods have been used to eliminate VOCs, including incineration, absorption, adsorption, condensation, and catalytic oxidation.[4–6] Among them, catalytic oxidation has been recognized as one of the most effective and economical ways for abating VOCs, as it has the advantages of low degradation temperature, high removal efficiency, and no secondary pollution.[4,7] To realize the industrial application of catalytic oxidation, the catalysts need to be developed extensively. So far, two types of traditional catalysts were researched deeply, including supported noble metals (such as Au, Pd, and Pt)[8,9] and transition metal oxides.[10,11] Although the former exhibits high activity and CO_x selectivity at low temperatures, the high cost and high sensitivity to water vapor, sulfur and chlorine compounds limit their applications. Transition metal oxides, such as Co_3O_4,[11,12] NiO,[13] MnO_x,[14] CuO,[15] and their composite oxides,[16–18] possess the advantages of low cost and high toxicity resistance. However, the reaction temperature for these catalysts is relatively high, which will affect their stability and increase energy costs.

In addition to these two types of catalysts, CeO_2 is also reported as an effective catalyst for the catalytic oxidation of VOCs as it has high oxygen storage capacity caused by its excellent redox properties. In recent years, CeO_2 with different morphologies and structures was researched for VOCs oxidation.[19,20] The catalytic activity of CeO_2 in the VOCs oxidation process can be improved by adding other elements to form composites, such as Mn, Cu, Ni and Co. The increment in catalytic performance may originate from the synergistic effect between CeO_2 and other metal oxides. The oxygen vacancy due to different electric states between Ce^{4+} and M^{x+} is another essential factor for the enhanced activity.[16,21] Thereinto, Ce–Mn composite oxides with tunable structure and size have been often used for VOCs oxidation because of the low costs, improved catalytic performances, and high thermal stability. For example, Wang *et al.* synthesized CeO_2–MnO_x and proved that the synergistic effect between Mn and Ce is the decisive factor on its excellent activity for benzene oxidation.[22] Zhao *et al.* prepared a series of Ce_aMnO_x microspheres with arbutus-like hierarchical structure by coprecipitation. The $Ce_{0.03}MnO_x$

[a]State Key Laboratory of Multiphase Complex Systems, Institute of Process Engineering, Chinese Academy of Sciences, Beijing 100190, China. E-mail: ybcui@ipe.ac.cn

[b]Key Laboratory of Cleaner Production and Integrated Resource Utilization of China National Light Industry, Beijing Technology and Business University, Beijing 100048, China

[c]School of Chemical Engineering, Shenyang University of Chemical Technology, Shenyang 110142, Liaoning, China

† Electronic supplementary information (ESI) available: Experimental details, XRD of SiO_2@CeO_2, SEM images of SiO_2 and $CeMnO_x$. See https://doi.org/10.1039/d2ra04678d

showed best catalytic activity for toluene oxidation with high stability and water resistance, due to the Mn^{4+} species and abundant surface oxygen.[23]

As 3D nano/micro-structured materials (including hollow nanospheres) possess high surface area and low density, they exhibit some advantages superior to corresponding bulk materials, which are beneficial for their application in catalysis, drug delivery, supercapacitors and so on.[23–27] Although little progress has been made in terms of synthesis and catalytic performance of CeO_2–MnO_x hollow nanospheres, the as-obtained materials could not possess homogeneous structure, including uniform morphology, diameter, and interior architecture.[28,29] In this paper, we prepared well-defined $CeMnO_x$ hollow nanospheres with different amounts of MnO_x by the combination of template method and interfacial reaction. Toluene was chosen as the target contaminant for catalytic oxidation. By tuning the content of MnO_x in the catalysts, the effect of Ce/Mn ratio on catalytic activity was evaluated. Our results demonstrated that $CeMnO_x$-3 with moderate content of Mn (15 wt%) showed low temperature for complete combustion of toluene (280 °C) and high stability for 36 h with toluene conversion above 97.7%. It also exhibited good water tolerance and recyclability under the condition of 5 vol% H_2O. Based on the study of catalysts, including structure, morphology, element states, and catalytic performance, the synergistic effect between Ce and Mn was proposed to play a critical role in the improvement of catalytic performance.

2 Experimental

The detailed Experimental section is described in the ESI.†

3 Results and discussion

3.1 Composition and structure

XRD was conducted to characterize the crystalline structures of as-prepared catalysts. As displayed in Fig. 1, the peaks for all the samples are similar and could be indexed to fluorite CeO_2 (JCPDS no. 34-0394) and no diffraction peak of MnO_x species is observed. Meanwhile, compared with the prominent reflection peaks (111 and 220) of CeO_2, a slight shift to higher Bragg angles is observed for the $CeMnO_x$ binary oxides. For the radius of Mn^{3+} (0.064 nm) and Mn^{4+} (0.060 nm) are smaller than those of Ce^{3+} (0.134 nm) and Ce^{4+} (0.114 nm), the spacing between crystal planes (d) of CeO_2 decreased when the manganese ions substituted cerium ions. Therefore, the value of θ for $CeMnO_x$ is calculated to be higher than that of CeO_2 from Bragg's law: $2d \sin\theta = k\lambda$.[30] This shift also illustrates that Mn has successfully migrated into the CeO_2 lattice through interfacial reaction due to the close contact between $Ce^{\delta+}$ and $Mn^{\delta+}$ during the calcination process. The introduction of Mn species could modify the crystallization of CeO_2, and form Mn–Ce solid solution. The difference in ionic radius means that the defects in the CeO_2 lattice are easily formed, including oxygen vacancies that can provide active centers for the creation of reactive oxygen species.[31]

The synthesis process of $CeMnO_x$ composite included three main steps and was illustrated in Scheme 1. Firstly, homogeneous SiO_2@CeO_2 was synthesized by the solvothermal method.[32–34] In this step, uniform SiO_2 spheres with a diameter of about 250 nm (Fig. S1 in the ESI†) were used as templates, and CeO_2 nanoparticles were covered on the surface of SiO_2 spheres by the self-assembly method. From XRD in Fig. S2,† we can see that the nanoparticles on SiO_2 were CeO_2 even though the broad diffraction peaks illustrate its low crystallinity, indicating CeO_2 could be obtained just after the solvothermal treatment of $Ce(NO_3)_3$ directly. In the second step, SiO_2@CeO_2 was dispersed in $KMnO_4$ solution to coat the MnO_x layer. Although most of Ce in SiO_2@CeO_2 existed in the form of Ce^{4+} with high valence, there was still a small amount of Ce^{3+} coming from the transformation of Ce^{4+} due to the excellent redox behavior of CeO_2. $KMnO_4$ with strong oxidation ability would oxidize this tiny amount of Ce^{3+} to CeO_2 and be reduced to MnO_x itself. This reaction can also be indirectly observed by the color change of the reaction system from purple to dark brown, corresponding to the color of MnO_4^- and MnO_x, respectively. In addition, the rough surface formed by the accumulation of CeO_2 nanoparticles in the first step could increase the contact between $KMnO_4$ and Ce(III) and accelerate the surface interaction. At last, the SiO_2 core was etched with NaOH solution and $CeMnO_x$ hollow spheres were obtained.

ICP-AES was used to ascertain the amount of Mn in the $CeMnO_x$ catalysts. The actual contents of Mn in $CeMnO_x$ catalysts increase with the concentration of $KMnO_4$ solution. It should be noticed that the preparation method involves the

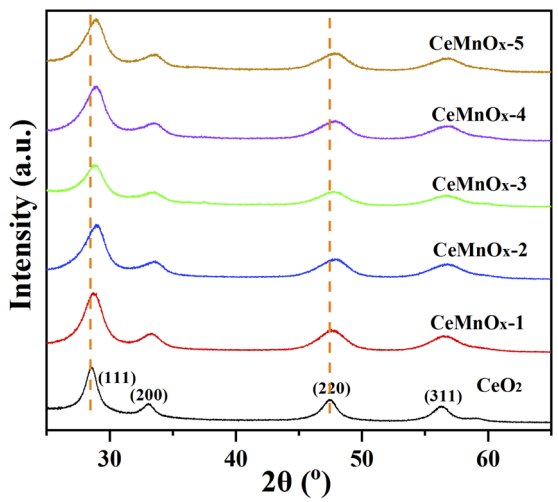

Fig. 1 XRD patterns of CeO_2 and the as-prepared $CeMnO_x$ hollow sphere catalysts.

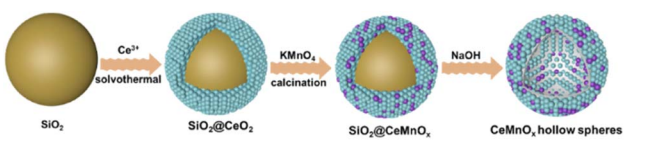

Scheme 1 Schematic illustration for the preparation of $CeMnO_x$ hollow spheres.

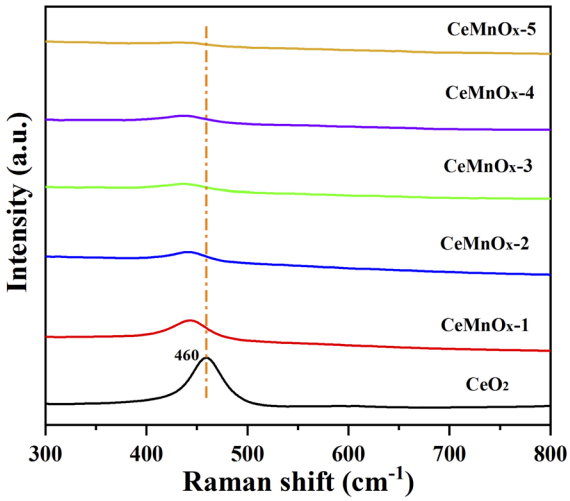

Fig. 2 Raman spectra of CeO_2 and the as-prepared $CeMnO_x$ catalysts.

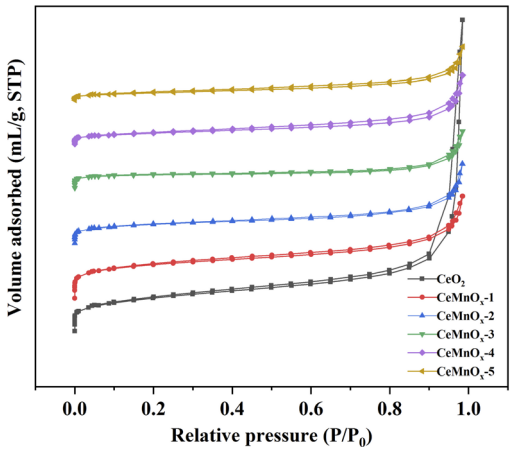

Fig. 3 N_2 adsorption/desorption isotherms curves of CeO_2 and the as-prepared $CeMnO_x$ catalysts.

oxidation of Ce^{3+} on the surface of CeO_2 with $KMnO_4$ to obtain MnO_x. As the amount of Ce^{3+} in CeO_2 is fixed, the content of MnO_x reaches saturation for $CeMnO_x$-4 (19.0%), which is close to sample 5, 18.90%.

Raman spectra of catalysts CeO_2 and the $CeMnO_x$ are shown in Fig. 2. The band at 460 cm^{-1} is assigned to the triply degenerated F_{2g} active mode of CeO_2, which reflects the symmetric breathing pattern of oxygen atoms around cerium ions in the fluorite CeO_2.[35] With the increase of Mn contents, the F_{2g} band shifts to lower wavenumbers (red shift) gradually, suggesting the variations of Ce–O bonding symmetry. The red shifts may attribute to the lattice contraction[36,37] and consequent oxygen vacancies,[38] which both originated from the partial incorporation of Mn ions with smaller radius into fluorite CeO_2. No Raman peaks for MnO_x species (*e.g.* Mn_3O_4) could be observed in the $CeMnO_x$ catalysts, which reveals that the MnO_x in the binary oxides is highly dispersed, in accordance with XRD results.[39–41]

N_2 adsorption–desorption isotherms of CeO_2 and $CeMnO_x$ are displayed in Fig. 3. All the catalysts present type II isotherms with H3-type hysteresis loops. According to IUPAC classification, these isotherms suggest the presence of slit-shaped micropores in the samples. The Brunauer–Emmett–Teller (BET) surface areas of the catalysts in Table 1 show an obvious downtrend (from 107.2 to 23.8 $m^2\ g^{-1}$) opposite to that of Mn content, indicating the addition of Mn leads to a more compact structure, which could be confirmed by SEM images in the following section.

As $CeMnO_x$-3 exhibited the best catalytic activity among all the $CeMnO_x$ catalysts, it was chosen as an example to study the morphologies by SEM and the images of other samples were given in Fig. S3.† The SiO_2@$CeMnO_x$-3 before NaOH treatment are composed of large-scale uniform and well-dispersed microspheres with 250–400 nm in diameter (Fig. 4a). The surfaces of the microspheres are rough and consists of small particles, indicating that CeO_2 nanoparticles has deposited on the SiO_2 templates successfully. After removing of SiO_2 templates with NaOH treatment, $CeMnO_x$-3 hollow spheres can be obtained (Fig. 4b), which inherit the morphologies of their precursors well. A few cracked spheres in Fig. 4b and c reveal their hollow features clearly. A high magnified SEM image of a ruptured $CeMnO_x$-3 microsphere in Fig. 4d reveals that the thickness of the hollow sphere is about 50 nm and the sphere is composed of abundant nanoparticles, contributing to a high specific surface area. For SiO_2@CeO_2 before NaOH treatment, the surfaces were composed of nanoparticles with 20 nm in diameter (Fig. S3a†). With careful observation, we can see that the SiO_2@CeO_2 nanospheres are loosely structured, with some areas showing a tendency to delaminate, indicating the weak interaction between the nanoparticles. For this reason, the shells of CeO_2 hollow sphere are fragile and easily to be broken after NaOH treatment, which is indicated by many broken spheres in Fig. S3b.† With the increase of Mn content, the ratio of broken spheres decreases and the surface of the spheres gets smoother and more compact, indicating the interaction between nanoparticles is enhanced, which is also the reason for the downward trend in the specific surface area (Fig. S3c–f†).

TEM images in Fig. 5a, e and i confirm the hollow character of the $CeMnO_x$ catalysts with uniform diameter and thickness, in consistent with the SEM images. From the TEM images of $CeMnO_x$-1 in Fig. 5b and c, we can see some large nanocrystals with high crystallinity on the surface. For $CeMnO_x$-3, large nanoparticles on the surface disappear and the structure of the sphere gets puffy (Fig. 5f and g). The thickness of the hollow sphere increases obviously from $CeMnO_x$-3 to $CeMnO_x$-5, and the structure becomes more compact (Fig. 5j). For the HRTEM images of the three catalysts, there is apparent lattice fringe with a spacing of about 0.31 nm, corresponding to the (111) plane of face-centered cubic CeO_2. No lattice fringe indexed to MnO_x species can be observed, but there are some areas with amorphous structure (marked with red circles in Fig. 5c, g and k), which attributes to part of Mn species that have not entered the CeO_2 lattice. We can see that there are more amorphous MnO_x particles that well dispersed on the surface of $CeMnO_x$-3 than those in $CeMnO_x$-1. But with a further increase of Mn content, $CeMnO_x$-5 is nearly covered by a layer of amorphous MnO_x

Table 1 Textural parameters of CeO_2 and $CeMnO_x$ catalysts

	CeO_2	$CeMnO_x$-1	$CeMnO_x$-2	$CeMnO_x$-3	$CeMnO_x$-4	$CeMnO_x$-5
Mn ratio[a] (%)	—	1.7	8.6	14.9	19.0	18.9
S_{BET} ($m^2\ g^{-1}$)	107.2	108.8	60.0	44.4	35.7	23.8

[a] Based on ICP results.

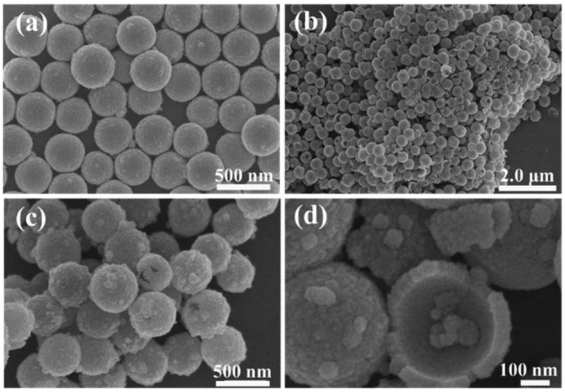

Fig. 4 SEM images of SiO_2@$CeMnO_x$-3 (a) and $CeMnO_x$-3 (b–d).

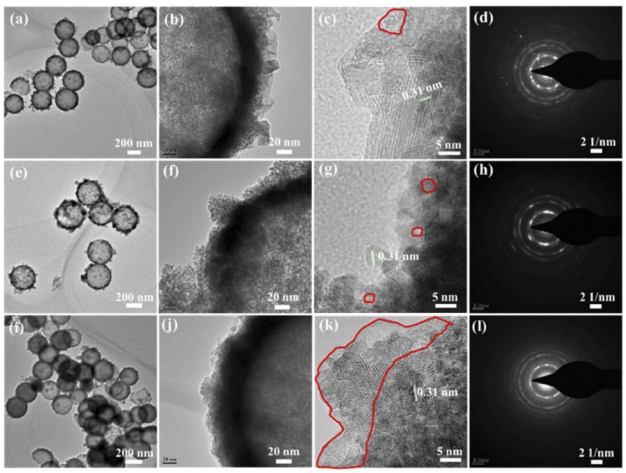

Fig. 5 TEM images and SAED patterns of $CeMnO_x$-1 (a–d), $CeMnO_x$-3 (e–h) and $CeMnO_x$-5 (i–l).

particles, illustrating the high amount of Mn (Fig. 5k). The diffraction points and rings in SAED in Fig. 5d prove the coexistence of pure CeO_2 and few $CeMnO_x$ with low crystallinity. For $CeMnO_x$-3, the diffraction points that indexed to CeO_2 was hard to be observed, further confirming the formation of a large amount of amorphous MnO_x on the surface of $CeMnO_x$ solid solution (Fig. 5h). The diffraction points disappeared totally for $CeMnO_x$-5, caused by the coverage of the MnO_x layer on CeO_2. The structural differences would affect the catalytic activity (Fig. 5l).

3.2 Chemical states of the catalysts

The chemical compositions of CeO_2 and $CeMnO_x$ were investigated by XPS (Fig. 6). Ce 3d spectra (Fig. 6a) are fitted to eight peaks by deconvolution and labelled as U and V, contributing to $3d_{5/2}$ and $3d_{3/2}$ spin–orbit components of Ce, respectively.[42,43] These peaks marked with V, V″, V‴, U, U″ and U‴ are attributed to the Ce^{4+} species while V′ and U′ are assigned to the Ce^{3+} species. The relative content of Ce^{3+} can be calculated by $Ce^{3+}/(Ce^{3+} + Ce^{4+})$ based on the peak area and the results are shown in Table 2. The relative surface Ce^{3+} content increases slightly, reaches a maximum for $CeMnO_x$-3. According to literatures, toluene catalytic oxidation on CeO_2 and MnO_x usually conforms to Mars–van-Krevelen (MvK) mechanism, in which oxygen atoms on the surface of the catalysts are key factors as they participate in the reaction.[38] So, the concentrations of oxygen vacancies and surface adsorbed oxygen species on the catalysts should be investigated deeply. Generally, nonstoichiometric Ce^{3+} species in CeO_2 leads to the generation of crystal defects and oxygen vacancies to maintain electrostatic balance following the reaction: $4Ce^{4+} + O^{2-} \rightarrow 4Ce^{4+} + 0.5O_2 + 2e^-/\square \rightarrow 2Ce^{4+} + 2Ce^{3+} + 0.5O_2 + \square$ ($\square$ represents oxygen vacancy).[38,44–47] Therefore, higher Ce^{3+} content indicates more oxygen vacancies, contributing to superior redox properties and excellent catalytic activity. The corresponding XPS spectra of Mn 2p for $CeMnO_x$ are deconvoluted into three main peaks with binding energies at 640.5, 641.7 and 643.0 eV (Fig. 6b), which are assigned to the spin–orbital of Mn^{2+}, Mn^{3+} and Mn^{4+} species, respectively. The results in Table 2 show that $CeMnO_x$-3 has the largest concentration of Mn with a lower valence state (52.5%). The existence of more Mn^{2+} and Mn^{3+} also imply the formation of more oxygen vacancies, similar to the effect of Ce^{3+}.

All the O 1s spectra in Fig. 6c can be deconvoluted into three peaks located at about 529.6, 530.5, and 533.1 eV, attributing to the lattice oxygen (O_I), adsorbed oxygen with low coordination (such as O_2^{2-}, O^{2-} and O^-, denoted as O_{II}), and carbonates (O_{III}), respectively.[40,48] The percentages of adsorbed oxygen for all the catalysts exhibit the same trend with Ce^{3+} and $Mn^{\delta+}$ with

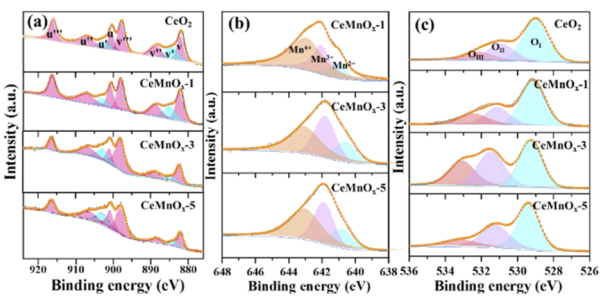

Fig. 6 XPS spectra of Ce 3d (a), Mn 2p (b) and O 1s (c) for CeO_2 and $CeMnO_x$-1, $CeMnO_x$-3 and $CeMnO_x$-5.

Table 2 The XPS fitting results of the catalysts

Catalysts	Surface element ratio (%)		
	$\frac{Ce^{3+}}{Ce^{3+}+Ce^{4+}}$	$\frac{Mn^{2+}+Mn^{3+}}{Mn^{2+}+Mn^{3+}+Mn^{4+}}$	$\frac{O_{II}}{O_I}$
CeO_2	14.6	—	48.8
$CeMnO_x$-1	16.9	41.0	49.3
$CeMnO_x$-3	20.9	52.5	88.5
$CeMnO_x$-5	19.5	49.5	61.4

lower valence states, consistent with the conclusion that Ce and Mn species with lower valence states are benefit for increasing the amount of surface adsorbed oxygen.[49] Strong interaction between Ce and Mn weakens the Ce–O bonds located at the interface of MnO_x and CeO_2, and increases the mobility of lattice oxygen. As a result, oxygen vacancies can be easily formed and surface adsorbed oxygen species are enhanced consequently, which are benefit for toluene oxidation according to the MvK mechanism.

3.3 Reducibility of the catalysts

Redox properties of the catalysts were investigated by H_2-TPR and the curves were exhibited in Fig. 7. CeO_2 exhibits a reduction peak at about 520 °C, which can be ascribed to the consumption of H_2 by CeO_2.[50] After the introduction of Mn, the reduction peaks of $CeMnO_x$-1 and $CeMnO_x$-2 shift to the lower temperature continually, implying that the introduction of Mn ions can improve the reduction reducibility of CeO_2 significantly. It should be noted that a broad band of H_2 consumption for $CeMnO_x$-2 began to occur at about 300 °C, which can be assigned to the reduction of MnO_x species.[36] With the increase of Mn content, $CeMnO_x$-3 exhibit three peaks at about 230, 285 and 354 °C, corresponding to the reduction of Mn^{4+} to Mn^{3+}, Mn^{3+} to Mn^{2+} and partial reduction of surface ceria, respectively.[50–52] For $CeMnO_x$-4 and $CeMnO_x$-5, even the peaks shift to high temperature again, they are still much lower than that of pure CeO_2. It is reported that –Mn–O–Ce– bond of $CeMnO_x$ hollow spheres can reduce the oxygen vacancy formation energy remarkably, and then strengthen the mobility of oxygen species from the bulk to the surface when compared with pure ceria.[53] These results indicate that the addition of an appropriate amount of Mn into the CeO_2 lattice can lead to high mobility and XPS results. Combined with all these results above, it is reasonable to speculate that the $CeMnO_x$ can exhibit better promote the release of the lattice oxygen, inconsistent with the catalytic activity than pure CeO_2, and $CeMnO_x$-3 should be the best one.

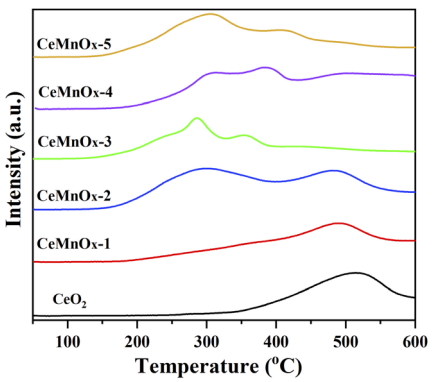

Fig. 7 H_2-TPR profiles of CeO_2 and the as-prepared $CeMnO_x$ catalysts.

3.4 Catalytic activity

The catalytic oxidation of toluene over the hollow structured $CeMnO_x$ catalyst is present in Fig. 8a. In general, the activities of all catalysts reveal a similar positive correlation with the reaction temperature. CeO_2 shows the lowest catalytic activity, whose T_{50} and T_{90} are as high as 310 and 369 °C, respectively. After the introduction of Mn, all the $CeMnO_x$ exhibit better performance than CeO_2, with the following order: $CeMnO_x$-3 > $CeMnO_x$-4 ≈ $CeMnO_x$-5 > $CeMnO_x$-2 > $CeMnO_x$-1 (deducing by T_{50} and T_{90}, marked with red lines in Fig. 8a). This result demonstrates that the introduction of Mn can improve the catalytic activities due to the synergistic effect between Ce and Mn. Especially for $CeMnO_x$-3, the complete conversion temperature of toluene is only 280 °C, while the conversion is only 8.9% for CeO_2 at the same temperature.

It is reported that with excess oxygen, the catalytic oxidation of toluene follows first-order kinetics with the toluene concentration.[34,54] When the toluene conversion is less than 20%, the ln r dependence of $1/T$ can be used to calculate apparent activation energies (Fig. 8b). For clarification, the reaction rates and activation energies calculated from the slope of the linear fit of the Arrhenius scatter plots were listed in Table 3. The reaction rate over $CeMnO_x$-3 is 0.141 μmol g^{-1} s^{-1}, the highest among these catalysts. E_a for $CeMnO_x$-3 is the lowest and increased with the order: $CeMnO_x$-3 < $CeMnO_x$-4 < $CeMnO_x$-2 < $CeMnO_x$-5 < $CeMnO_x$-1 < CeO_2. The highest reaction rate and lowest E_a value for $CeMnO_x$-3 both confirm its excellent performance on toluene oxidation.

3.5 Structure–activity relationships

The activation ability of oxygen molecules for catalysts is an essential factor in evaluating their catalytic activity. It has been proved that the surface oxygen vacancies are favourable for the

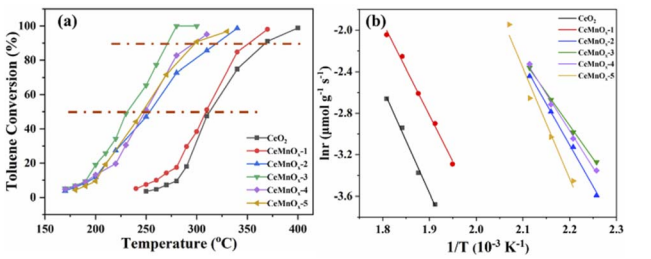

Fig. 8 (a) Toluene conversions as a function of reaction temperature and (b) Arrhenius linear fit plots for toluene oxidation over the catalysts.

Table 3 r and E_a for toluene combustion over CeO_2 and $CeMnO_x$ catalysts

Catalysts	r^a (μmol g^{-1} s^{-1})	E_a (kJ mol^{-1})
CeO_2	0.025	84
$CeMnO_x$-1	0.055	79
$CeMnO_x$-2	0.087	66
$CeMnO_x$-3	0.141	51
$CeMnO_x$-4	0.097	59
$CeMnO_x$-5	0.070	71

[a] The values of r for CeO_2 and $CeMnO_x$-1 were obtained at 250 °C and the others were obtained at 200 °C.

adsorption and activation of O_2.[37] Therefore, the catalysts with high oxygen vacancies may exhibit good catalytic performance. XPS spectra (Fig. 6) confirm that after the addition of Mn, the content of Ce^{3+} species increase and give rise to more oxygen vacancies, favourable for the activation of O_2. Accordingly, O 1s spectra of $CeMnO_x$ confirm the existence of more surface-absorbed oxygens compared with CeO_2, which would increase the redox property of $CeMnO_x$ catalysts significantly. According to the MvK mechanism, O_{latt} (O^{2-}) on the surface of the catalyst are the active species. After being consumed of O^{2-} in the oxidation, they can be regenerated by migration of electrophilic surface-absorbed oxygens (O_2^{2-}, O^{2-} and O^-) into oxygen vacancies with the dissociation of O_2 in the feed continually (Scheme 2). Therefore, $CeMnO_x$-3 with the most Ce^{3+} species and surface-absorbed oxygens showed the best catalytic activity. However, when Mn continues to increase, the surface MnO_x species would increase while the Ce^{3+} content decreases gradually (Table 2). From Fig. 5k, there was even a layer of amorphous MnO_x that covered the solid solution $CeMnO_x$, inhibiting the contact between –Mn–O–Ce– and O_2. Therefore, the surface-absorbed oxygens and catalytic activity decreased correspondingly.

3.6 The stability test and water resistance

The stability of the catalysts is also a critical factor for practical application. Fresh $CeMnO_x$-3 was tested for the toluene conversion (inlet concentration 1000 ppm) as a function of time on stream at 280 °C. As shown in Fig. 9a, the catalyst was relatively stable for 10 h, with 100% toluene conversion. In the next 10 h, the conversion only exhibits a slight decrease, and is stable at 99%. After reacting for 20 h, the reaction system was cooled to room temperature and reheated to 200 °C for reusability test. It can be seen that in the second cycle, there is no apparent change in toluene conversion. Even after the third test, the toluene conversion can maintain 97.7%. Obviously, the catalyst has excellent catalytic stability and reusability for the oxidation of toluene, endowing it the possibility of future industrialization.

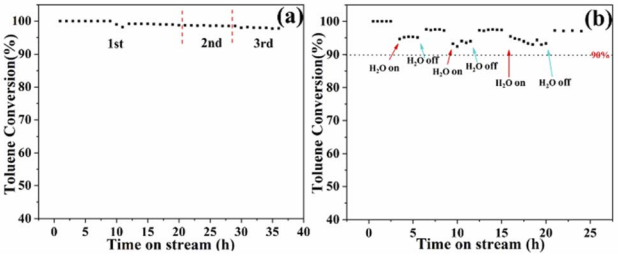

Fig. 9 Catalytic stability without (a) and with (b) water (10 vol%) of $CeMnO_x$-3 for toluene oxidation at 280 °C.

In practical application, moisture tolerance of the catalyst is another important factor to be considered as VOCs gas in the industry often contains water. Therefore, the influence of vapor on the long-term catalytic activity of $CeMnO_x$-3 under the feed gas stream including 5 vol% of water at 280 °C was investigated and the result was given in Fig. 9b. In the absence of water vapor, the toluene conversion maintained 100%, consistent with the results in Fig. 9a. After introducing water vapor into the reaction stream, the toluene conversion decreased to 95% directly and remained stable afterward. Once the water vapor was stopped, the conversion recovered to 97%. For the subsequent two cycles, the catalytic activity showed a similar trend and the toluene conversion was above 90% throughout the test. Finally, the toluene conversion could recover to 97% after the water vapor was out. Therefore, the catalyst owned excellent water vapor tolerance, which is a favorable factor for achieving industrial application.

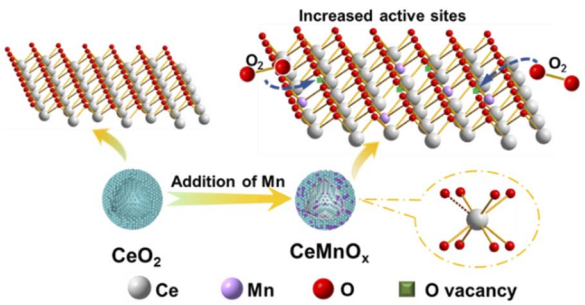

Scheme 2 Schematic illustration for the synergy effect of Ce and Mn in the $CeMnO_x$ catalyst.

4 Conclusions

In this work, we combined the template method and interfacial reaction to prepare a series of $CeMnO_x$ binary oxide hollow spheres with uniform morphology, diameter and thickness. Mn was incorporated by an interfacial redox reaction between $KMnO_4$ and Ce elements with low valence on the surface of SiO_2@CeO_2. The as-prepared binary oxides exhibit better catalytic activities than CeO_2 hollow spheres. $CeMnO_x$-3 exhibits the lowest T_{90} (nearly 100 °C lower than that of CeO_2), excellent stability and H_2O resistance even with WHSV of 120 000 h^{-1}. Redox properties and surface oxygen vacancies of the binary oxide catalysts are improved as the addition of Mn would cause strong interaction between Ce and Mn, increasing of surface-adsorbed oxygen species, which are critical to the enhanced catalytic performance.

Author contributions

Yuhua Zheng: methodlogy, analysis, writing and editing. Jing Zhou: synthesis. Xi Zeng and Dandan Hu, investigation and characterization. Fang Wang: data curation. Yanbin Cui: supervision, funding acquisition and review.

Conflicts of interest

There are no conflicts to declare.

Acknowledgements

This work is financially supported by the financial support from National Natural Science Foundation of China (No. 22076189) and the Open Research Fund Program of Key Laboratory of Cleaner Production and Integrated Resource Utilization of China National Light Industry (No. CP2021YB06).

References

1 B. J. FinlaysonPitts and J. N. Pitts, *Science*, 1997, **276**, 1045–1052.
2 S. Kim, R. Vermeulen, S. Waidyanatha, B. A. Johnson, Q. Lan, M. T. Smith, L. Zhang, G. Li, M. Shen, S. Yin, N. Rothman and S. M. Rappaport, *Cancer Epidemiol., Biomarkers Prev.*, 2006, **15**, 2246–2252.
3 M. Amann and M. Lutz, *J. Hazard. Mater.*, 2000, **78**, 41–62.
4 Y. Guo, M. Wen, G. Li and T. An, *Appl. Catal., B*, 2021, **281**, 119447.
5 G. R. Parmar and N. N. Rao, *Crit. Rev. Environ. Sci. Technol.*, 2009, **39**, 41–78.
6 X. Zhang, B. Gao, A. E. Creamer, C. Cao and Y. Li, *J. Hazard. Mater.*, 2017, **338**, 102–123.
7 C. He, J. Cheng, X. Zhang, M. Douthwaite, S. Pattisson and Z. Hao, *Chem. Rev.*, 2019, **119**, 4471–4568.
8 S. Scire and L. F. Liotta, *Appl. Catal., B*, 2012, **125**, 222–246.
9 L. F. Liotta, *Appl. Catal., B*, 2010, **100**, 403–412.
10 H. Liu, X. Li, Q. G. Dai, H. L. Zhao, G. T. Chai, Y. L. Guo, Y. Guo, L. Wang and W. C. Zhan, *Appl. Catal., B*, 2021, **282**, 9.
11 K. W. Zha, W. J. Sun, Z. Huang, H. L. Xu and W. Shen, *ACS Catal.*, 2020, **10**, 12127–12138.
12 X. Y. Wang, Y. Liu, T. H. Zhang, Y. J. Luo, Z. X. Lan, K. Zhang, J. C. Zuo, L. L. Jiang and R. H. Wang, *ACS Catal.*, 2017, **7**, 1626–1636.
13 H. C. Wang, W. Q. Guo, Z. Jiang, R. O. Yang, Z. Jiang, Y. Pan and W. F. Shangguan, *J. Catal.*, 2018, **361**, 370–383.
14 S. C. Kim and W. G. Shim, *Appl. Catal., B*, 2010, **98**, 180–185.
15 X. L. Meng, L. K. Meng, Y. J. Gong, Z. H. Li, G. Mo and J. Zhang, *RSC Adv.*, 2021, **11**, 37528–37539.
16 S. Y. Feng, J. D. Liu and B. Gao, *Chem. Eng. J.*, 2022, **429**, 12.
17 J. Y. Yun, L. K. Wu, Q. L. Hao, Z. H. Teng, X. Gao, B. J. Dou and F. Bin, *J. Environ. Chem. Eng.*, 2022, **10**, 8.
18 Y. Q. Zeng, K. G. Haw, Z. G. Wang, Y. A. Wang, S. L. Zhang, P. Hongmanorom, Q. Zhong and S. Kawi, *J. Hazard. Mater.*, 2021, **404**, 7.
19 Q. Y. Wang, K. L. Yeung and M. A. Banares, *Catal. Today*, 2020, **356**, 141–154.
20 M. A. Salaev, A. A. Salaeva, T. S. Kharlamova and G. V. Mamontov, *Appl. Catal., B*, 2021, **295**, 38.
21 S. Zhang, H. Z. Wang, H. Y. Si, X. Q. Jia, Z. Y. Wang, Q. Li, J. Kong and J. B. Zhang, *ACS Appl. Mater. Interfaces*, 2020, **12**, 40285–40295.
22 Z. Wang, G. L. Shen, J. Q. Li, H. D. Liu, Q. Wang and Y. F. Chen, *Appl. Catal., B*, 2013, **138**, 253–259.
23 L. L. Zhao, Z. P. Zhang, Y. S. Li, X. S. Leng, T. R. Zhang, F. L. Yuan, X. Y. Niu and Y. J. Zhu, *Appl. Catal., B*, 2019, **245**, 502–512.
24 W. Stober, A. Fink and E. Bohn, *J. Colloid Interface Sci.*, 1968, **26**, 62–69.
25 Z. H. Li, V. Ravaine, S. Ravaine, P. Garrigue and A. Kuhn, *Adv. Funct. Mater.*, 2007, **17**, 618–622.
26 W. Y. Ko, L. J. Chen, Y. H. Chen, W. H. Chen, K. M. Lu, J. R. Yang, Y. C. Yen and K. J. Lin, *J. Phys. Chem. C*, 2013, **117**, 16290–16296.
27 S. S. Acharyya, S. Ghosh and R. Bal, *ACS Appl. Mater. Interfaces*, 2014, **6**, 14451–14459.
28 W. Liu, S. N. Wang, R. Y. Cui, Z. X. Song and X. J. Zhang, *Microporous Mesoporous Mater.*, 2021, **326**, 111370.
29 C. Zhu, S. N. Guan, W. Z. Li, A. T. Ogunbiyi, K. Chen and Q. Zhang, *ACS Omega*, 2021, **6**, 35404–35415.
30 J. Zhang, Y. D. Cao, C. A. Wang and R. Ran, *ACS Appl. Mater. Interfaces*, 2016, **8**, 8670–8677.
31 L. Li, C. Y. Zhang, F. Chen, Y. T. Xiang, J. L. Yan and W. Chu, *Catal. Today*, 2021, **376**, 239–246.
32 L. H. Hu, Q. Peng and Y. D. Li, *J. Am. Chem. Soc.*, 2008, **130**, 16136–16137.
33 L. F. Liotta, H. J. Wu, G. Pantaleo and A. M. Venezia, *Catal. Sci. Technol.*, 2013, **3**, 3085–3102.
34 S. S. Acharyya, S. Ghosh, R. Tiwari, B. Sarkar, R. K. Singha, C. Pendem, T. Sasaki and R. Bal, *Green Chem.*, 2014, **16**, 2500–2508.
35 B. Fazio, L. Spadaro, G. Trunfio, J. Negro and F. Arena, *J. Raman Spectrosc.*, 2011, **42**, 1583–1588.
36 P. Venkataswamy, D. Jampaiah, K. N. Rao and B. M. Reddy, *Appl. Catal., A*, 2014, **488**, 1–10.
37 F. Y. Hu, J. J. Chen, S. Zhao, K. Z. Li, W. Z. Si, H. Song and J. H. Li, *Appl. Catal., A*, 2017, **540**, 57–67.
38 X. T. Lin, S. J. Li, H. He, Z. Wu, J. L. Wu, L. M. Chen, D. Q. Ye and M. L. Fu, *Appl. Catal., B*, 2018, **223**, 91–102.
39 J. Mondal, P. Borah, S. Sreejith, K. T. Nguyen, X. G. Han, X. Ma and Y. L. Zhao, *ChemCatChem*, 2014, **6**, 3518–3529.
40 S. Ghosh, S. S. Acharyya, S. K. Sharma and R. Bal, *Catal. Sci. Technol.*, 2016, **6**, 4644–4654.
41 J. M. Chalmers and P. R. Griffiths, *Handbook of Vibrational Spectroscopy*, John Wiley & Sons Ltd., West Sussex, 2002.
42 S. H. Xie, Y. X. Liu, J. G. Deng, X. T. Zhao, J. Yang, K. F. Zhang, Z. Han and H. X. Dai, *J. Catal.*, 2016, **342**, 17–26.
43 G. L. Zhou, H. R. Liu, K. K. Cui, A. P. Jia, G. S. Hu, Z. J. Jiao, Y. Q. Liu and X. M. Zhang, *Appl. Surf. Sci.*, 2016, **383**, 248–252.
44 K. Wang, Y. Q. Chang, L. Lv and Y. Long, *Appl. Surf. Sci.*, 2015, **351**, 164–168.

45 C. J. Ma, Y. Y. Wen, Q. Q. Yue, A. Q. Li, J. L. Fu, N. W. Zhang, H. J. Gai, J. B. Zheng and B. H. Chen, *RSC Adv.*, 2017, **7**, 27079–27088.
46 R. L. Mi, D. Li, Z. Hu and R. T. Yang, *ACS Catal.*, 2021, **11**, 7876–7889.
47 X. W. Liu, K. B. Zhou, L. Wang, B. Y. Wang and Y. D. Li, *J. Am. Chem. Soc.*, 2009, **131**, 3140–3141.
48 H. Pan, Y. F. Jian, C. W. Chen, C. He, Z. P. Hao, Z. X. Shen and H. X. Liu, *Environ. Sci. Technol.*, 2017, **51**, 6288–6297.
49 P. Venkataswamy, K. N. Rao, D. Jampaiah and B. M. Reddy, *Appl. Catal., B*, 2015, **162**, 122–132.
50 T. Y. Li, S. J. Chiang, B. J. Liaw and Y. Z. Chen, *Appl. Catal., B*, 2011, **103**, 143–148.
51 S. Y. Ding, C. Zhu, H. Hojo and H. Einaga, *J. Hazard. Mater.*, 2022, **424**, 11.
52 H. Sun, X. L. Yu, X. Y. Ma, X. Q. Yang, M. Y. Lin and M. F. Ge, *Catal. Today*, 2020, **355**, 580–586.
53 P. F. Zhang, H. F. Lu, Y. Zhou, L. Zhang, Z. L. Wu, S. Z. Yang, H. L. Shi, Q. L. Zhu, Y. F. Chen and S. Dai, *Nat. Commun.*, 2015, **6**, 10.
54 J. Kirchnerova, M. Alifanti and B. Delmon, *Appl. Catal., A*, 2002, **231**, 65–80.